

SKA-LOW SIMULATIONS FOR A COSMIC DAWN/EPOCH OF REIONISATION DEEP FIELD

ANNA BONALDI^{1,*}, PHILIPPA HARTLEY¹, SIMON PURSER¹, OMKAR BAIT¹, EUNSEONG LEE^{2,3}, ROBERT BRAUN¹, FLORENT MERTENS^{4,5}, ANDREA BRACCO^{6,7}, WENDY WILLIAMS¹, AND CATH TROTT^{8,9}

¹SKA Observatory, Jodrell Bank, Lower Whittington, Macclesfield, SK11 9FT, UK

²Jodrell Bank Centre for Astrophysics, School of Physics and Astronomy, University of Manchester, Oxford Road, Manchester M13 9PL, U.K.

³Department of Physics and Astronomy, University of Pennsylvania, Philadelphia, PA 19104, U.S.A.

⁴LUX, Observatoire de Paris, PSL Research University, CNRS, Sorbonne Université, F-75014 Paris, France

⁵Kapteyn Astronomical Institute, University of Groningen, PO Box 800, 9700 AV Groningen, The Netherlands

⁶INAF – Osservatorio Astrofisico di Arcetri, Largo E. Fermi 5, 50125 Firenze, Italy

⁷Laboratoire de Physique de l'Ecole Normale Supérieure, ENS, Université PSL, CNRS, Sorbonne Université, Université de Paris, F-75005 Paris, France

⁸International Centre for Radio Astronomy Research, Curtin University, Bentley WA, Australia and

⁹ARC Centre of Excellence for All-Sky Astrophysics in 3D, Australia

Version 16th February 2026

Abstract

We present a realistic simulation of an SKA-Low cosmic dawn/epoch of reionisation (CD/EoR) observation, which can be used to further the development of foreground-mitigation approaches. The simulation corresponds to a deep (1000 h) integration of a single pointing over the 106 MHz–196 MHz frequency range. The sky components include the CD/EoR signal, extragalactic foreground emission featuring strong (over 5 Jy at 150 MHz) out-of-field sources and in-field sources down to $1 \mu\text{Jy}$ at 150 MHz, and Galactic emission from the GSM2016 model complemented with small-scales structure beyond its native ~ 1 deg resolution from a magneto-hydrodynamic simulation of the interstellar medium. Modeled errors include a partial de-mixing of the out-of-field sources, direction-dependent calibration errors leading to residual ionospheric effects, and direction-independent gain calibration errors, on top of thermal noise. Simulated observations are delivered as visibilities as well as imaging products with natural weighting. The true, uncorrupted, CD/EoR signal is also delivered, to allow an assessment of the efficacy of foreground-mitigation approaches. The codes used to generate these simulations are also delivered, so that new simulated datasets can be produced. This simulation has been the basis for the SKA Science Data Challenge 3a (SDC3a), which addressed foreground removal.

Keywords: astro-ph.CO (Physics - Cosmology and Extragalactic Astrophysics), astro-ph.IM (Physics - Instrumentation and Methods for Astrophysics)

1. INTRODUCTION

The detection of the 21 cm line from neutral hydrogen (HI) during the cosmic dawn (CD) and the epoch of reionisation (EoR) is a high priority science objective for the Square Kilometre Array Observatory (SKAO, [Koopmans et al. 2015](#)) and is being actively pursued by total power ([EDGES Bowman et al. 2008, 2018](#); [SARAS Singh et al. 2017](#); [Jishnu Nambissan et al. 2021](#)) and interferometric (GMRT [Paciga et al. 2011](#); PAPER [Kolonis et al. 2019](#); LOFAR [Patil et al. 2017](#); [Mertens et al. 2020](#); MWA [Barry et al. 2019](#); [Li et al. 2019](#); [Trott et al. 2020](#); Ewall-Wice et al. 2016; [Yoshiura et al. 2021](#); HERA [Abdurashidova et al. 2022](#); OVRO-LWA [Eastwood et al. 2019](#); [Garsden et al. 2021](#); NenuFAR; [Munshi et al. 2024](#)) experiments.

During the CD, one of the least explored epochs of the Universe, starting at $z \sim 30$ ($\nu \sim 45$ MHz) the neutral hydrogen provides a unique probe of the emergence of the first luminous sources and their impact on the surrounding medium. Subsequently, during the epoch

of reionisation (EoR) tracking the abundance of HI at $\nu \sim 100$ –250 MHz ($z \sim 13$ –4.7) gives us a detailed account on when and how the Universe globally transitioned from neutral to ionised.

So far, the detection has been elusive, although great progress has been made on upper limits to the signal ([Trott & Pober 2019](#), and references therein). One of the biggest challenges is the presence of radio emission from sources along the line of sight, due to external galaxies as well as our Milky Way, three to four orders of magnitude brighter than the signal of interest. This foreground emission needs to be strongly mitigated (with either subtraction or avoidance methods) before any measurement of the CD/EoR signal can be made (see [Chapman & Jelić 2019](#), for a review).

Foreground emission, dominated by synchrotron and free-free processes, exhibits an intrinsically smooth frequency behavior, whereas the 21-cm signal from the EoR typically decorrelates over a few MHz. This fundamental difference underpins many of the foreground removal methods developed in recent years (e.g. [Chapman et al. 2015](#); [Mertens et al. 2024](#), and references therein).

* E-mail: anna.bonaldi@skao.int

These methods have been shown to perform well in simulations. However, the real challenge arises when instrumental and environmental effects are taken into account. The chromaticity of the instrument, both in the point spread function and in the primary beam (Trott & Wayth 2016; Ewall-Wice et al. 2017; Wilensky et al. 2024; Chokshi et al. 2024) separates smooth-spectrum foregrounds from frequency-dependent structures, making them much harder to isolate and subtract. Additional complications such as ionospheric fluctuations (Trott et al. 2018; Brackenhoff et al. 2024; Pal et al. 2025; Hodgson & Johnston-Hollitt 2026), Radio-Frequency Interference (RFI, e.g. Wilensky et al. 2023), and imperfect calibration can further distort the spectral behavior of foregrounds, introducing features that mimic or obscure the EoR signal. Achieving the accuracy needed for reliable detection therefore requires a joint treatment of foreground characterization and instrumental calibration (e.g. Barry et al. 2016).

In this work we aim to bring simulation work close to the realistic scenario, by providing a detailed simulation of an SKA-Low EoR observation. Our simulation includes both diffuse and point-like foreground contamination, as well as the residual effect of out-of-field strong sources that enter the field of view (FoV) due to the telescope’s sidelobes. We further model ionospheric effects and calibration errors.

This is the most sophisticated SKA-Low EoR simulation produced to date, and we make it available, together with the codes used to produce it, as a benchmark against which foreground mitigation approaches can be tested and refined. This simulation has been the basis for the SKA science data challenge 3a (SDC3a, Bonaldi et al. 2025), an EoR foreground mitigation exercise undertaken by the SKA science community in preparation for the advent of the SKA data.

This paper is organized as follows. In Sec. 2 we describe the telescope model adopted to mimic the response of the SKA-Low array; in Sec.3 we describe the model of the sky, including point-like and diffuse foregrounds and the CD/EoR signal; in Sec.4 we describe the error model, which includes corrupting effects introduced in the data. Sec.5 describes the simulation outputs that we are making available; finally, conclusions are drawn in Sec.7. This paper is accompanied by data and of codes repositories, as specified in Sec. 8.

2. TELESCOPE MODEL

We simulate full visibility data using the OSKAR¹ (Dulwich et al. 2009) package. OSKAR makes use of a telescope model, containing the details of all antennas/stations, and a sky model, containing a list of all the sources in the sky. There is provision to include a variety of instrumental errors into the simulation, which we refer to as the error model.

The parameters adopted for the OSKAR simulation are as follows:

- field centre (RA,Dec) = (00h, -30deg);
- 106–196 MHz frequency range with frequency sampling of 100 kHz. The chosen frequency range

tracks the redshifted 21 cm line in the redshift range of $z = 6.2$ –12.4;

- 4 h track duration sampled with a 10 s integration time;
- thermal noise level consistent with an integration time of 1000 h.

The choice of field is somewhat arbitrary and has not been optimised for an EoR observation. Sky components are mostly based on simulations, and therefore do not accurately represent the chosen area of the sky (see Sec.3 for more details).

The telescope model makes use of the SKA-Low configuration of 512 stations (Dewdney & Braun 2016). The u, v coverage corresponding to this configuration is shown in Fig. 1. This configuration has a maximum baseline of $B_{\max} \sim 74$ km which corresponds to a maximum spatial resolution of Full Width at Half Maximum (FWHM) ~ 10 arcsec in the frequency range explored here.

The station layout is the so-called *Vogel* layout, a one arm spiral configuration with a uniform areal density of the 256 dual-polarisation antennas and a maximally diverse azimuthal sampling (Vogel 1979). This is distinct from the “perturbed Vogel” layout that is actually being deployed within SKA-Low, in which a degree of randomisation has been added to the areal sampling. Only a single station layout has been adopted in our simulation to reduce computational expense, rather than a full set of 512 diverse station layouts. The implication is that the effective station beam for all visibilities is simply the auto-correlation beam of this one station layout. The most important consequence of this simplification is an elevated far side-lobe response. An attempt to compensate for this effect is made within the sky model definition (see Sec. 3 for more details). The OSKAR code already supports use of distinct station layouts throughout, so this could be adopted if a more realistic station beam response was desired for each simulated visibility.

The voltage response pattern of each antenna within each station has also been assumed to be the OSKAR default, a half-wavelength (at each observing frequency) dipole pattern with a North-South/East-West orientation of the X/Y polarisations, in order to minimise computational expense. In reality, the embedded element voltage patterns within the SKA-Low stations are known to have significant variability in their shape that has a strong frequency dependence due to the varying degree of inter-antenna coupling between nearby antennas, while the intrinsic X/Y antenna polarisations have been given a distinctly different orientation within each of the 512 stations rather than being co-aligned with the cardinal directions. Nominal X/Y polarisation response will be determined during digital beam-forming for each station from this local X/Y starting point. Work is currently underway to embed realistic embedded element patterns for SKA-Low within the OSKAR code, which would permit more realistic simulations to be undertaken.

3. SKY MODEL

The sky components described in this Section are explicitly designed as a plausible realisation of the true sky rather than a prediction for the simulated field. This was

¹ <https://ska-telescope.gitlab.io/sim/oskar/>

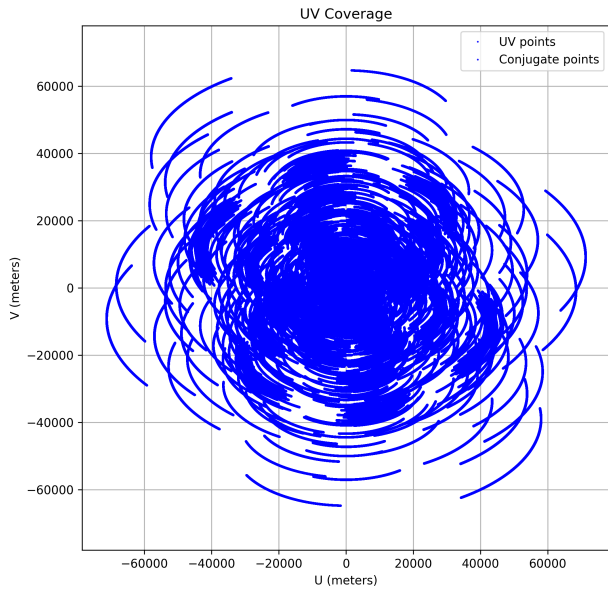


Figure 1. u, v coverage corresponding to the simulated observation.

done on purpose to ensure a blind foreground mitigation exercise. Some real data has been used, as noted below.

OSKAR makes use of a sky model consisting of a list of sources modeled spatially as 2D Gaussians and spectrally as power laws. Although this might appear like a severe limitation, there are strategies that allow a much more general model of the sky to be used as an input. To overcome the power-law approximation for the frequency behaviour of the components, our sky model has been generated for each frequency channel, so that any frequency behaviour is accurately tracked.

To introduce spatially diffuse components, we have produced gridded maps with an appropriate pixel size. Each pixel in the gridded representation has then been input as a Gaussian source model component in **OSKAR**. We have used gridded representations for the EoR and the Galactic foregrounds, that are spatially diffuse, but also for the cumulative contribution from faint extragalactic sources. This has been done to reduce the computational cost of the simulation, which depends on the number of **OSKAR** sky model sources. As a compromise between accuracy and computational complexity, we have adopted two grids:

- *Fine grid*: 5760×5760 pixels, which gives a 5×5 arcsec pixel sampling over the FoV area. This cube was smoothed with a 10×10 arcsec FWHM gridding kernel and pixels from this grid were used in **OSKAR** as Gaussian source model components of 10×10 arcsec extent with a flux density of the pixel brightness.
- *Coarse grid*: 512×512 pixels, which gives a 56.25×56.25 arcsec pixel sampling over the FoV area. This cube was smoothed to an effective resolution of 112×112 arcsec and pixels from this grid

were used in **OSKAR** as Gaussian source model components with spatial extent of 112×112 arcsec and flux density of the pixel brightness.

Below we list all the sky components and the way they have been modelled in **OSKAR**.

3.1. Extragalactic sources

3.1.1. Out-of-field sources

Sources that are bright enough for their contribution to be significant near the pointing direction even when entering the field through the telescope’s far sidelobes were included over the full 2π steradians above the horizon at any time. In this category are both the so-called “A-Team” sources that are brighter than a few 100 Jy at 200 MHz as well as all sources brighter than 5 Jy at 150 MHz (about 1200 in number) from the Lynch et al. (2021) composite GLEAM and LoBES catalogue. These sources were all included individually as **OSKAR** components, represented by an elliptical Gaussian approximation spatially and with a frequency-dependent flux density determined from an amplitude and spectral index defined at some reference frequency.

3.1.2. In-field sources

In-field extragalactic sources have been included in numbers consistent with a sample complete down to $1 \mu\text{Jy}$ at 150 MHz over a spatial extent of 8×8 degrees centred on the pointing direction. The strongest sources (above 100 mJy at 150 MHz) are from the Lynch et al. (2021) catalogue mentioned previously and were inserted as individual **OSKAR** components.

Sources with $1 \mu\text{Jy} \leq I_{150\text{MHz}} < 100 \text{mJy}$ are from a simulated catalogue obtained with the T-RECS² (Bonaldi et al. 2023, 2019) code. The T-RECS catalogue was converted to an image cube of 5×5 arcsec pixel size with a dedicated code³ which represents resolved star-forming galaxies as exponential Sersic profiles, steep-spectrum AGN with a library of real AGN images, flat-spectrum AGN and unresolved sources with a Gaussian representation. Pixels in this gridded representation exceeding 10^{-5}Jy/pixel (some 154,000 in number) were used in the fine grid; the remaining ones were spatially smoothed to an effective resolution of 112×112 arcsec and included in the coarse grid.

In figure 2 we show the number counts of the sources at 150 MHz, their provenance, and the way that they were modeled within **OSKAR**. In total we have more than 15 million sources, which motivated the use of a gridded representation for the fainter sources, to reduce the computational complexity of the simulation.

3.2. Galactic diffuse emission

Our Galactic diffuse total emission is based on the Galactic Sky Model 2016 (GSM2016, Zheng et al. 2017), evaluated at each observing frequency towards the specified pointing centre. The PyGDSM implementation⁴ (Price 2016) of this sky model relies on a linear interpolation in $\log(\text{frequency})$ between the reference frequencies

² <https://github.com/abonaldi/TRECS>

³ <https://github.com/abonaldi/SKA0-SDC>

⁴ <https://github.com/telegraphic/pygdsM>

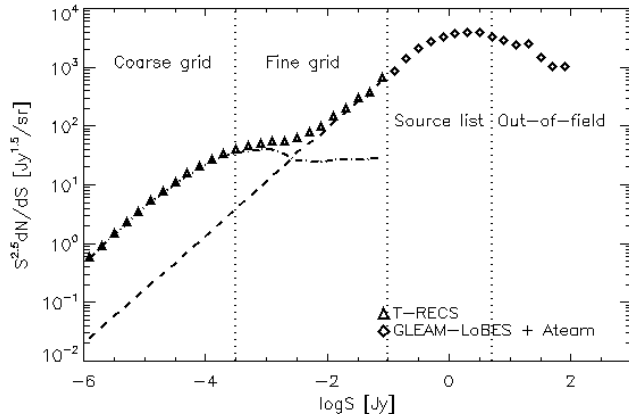


Figure 2. Differential source counts for the extragalactic sources inserted in the simulation. We also indicated the flux limits used for the out-of-field sources, the sources included as a source list, and those included as a coarse and fine grid. For the T-RECS sources (triangles) the counts are also shown separately for AGN (dashed line) and SFGs (dash-dotted line). In total we included over 15 million sources.

of the model (specifically 85, 150, and 408 MHz for our case). We modified this code to instead provide a quadratic interpolation in $\log(\text{frequency})$ in order to eliminate discontinuous derivatives within our band. The GSM2016 model is limited in its effective angular resolution by the native resolution of the all-sky observations that it employs. At the low radio frequencies of relevance for this work, this is about 1 degree. We have supplemented our model of the Galactic foreground emission by including total synchrotron emission at the relevant radio frequencies from a magneto-hydrodynamical (MHD) simulation (Bracco et al. 2022) of a hundreds-of-parsec wide Galactic volume sampled with 512×512 pixels. These synthetic data, derived from Ntormousi et al. (2017), represent a realistic model of a shock-driven turbulent, magnetized, and multiphase interstellar medium, whose dynamics are affected by stellar feedback. The spatial frequency content of the GSM2016 and MHD sky models was merged using the `miriad`⁵ (Sault et al. 1995) package task `immerge` with a normalisation at overlapping spatial scales, that was tied to the GSM2016 sky model at each frequency. In this way, filamentary structures in the Galactic foreground model were extended into the arcmin regime and the result was scaled to units of Jy/pixel. The Galactic diffuse emission was added to the coarse grid.

3.3. Cosmic Dawn and Epoch of Reionisation

Finally, a 21cmFAST⁶ (Murray et al. 2020; Mesinger et al. 2011) simulation of the Cosmic Dawn and Epoch of Reionisation (CD/EoR) was generated. We have adopted 21cmFAST version 3.2.0 and Planck18 cosmology $\Omega_m = 0.30964$, $\Omega_\Lambda = 0.69036$, $H_0 = 67.66$. The 21cmFAST reionisation parameters and the corresponding Brightness temperature are shown in Figure 3. This

⁵ <https://www.atnf.csiro.au/computing/software/miriad/>

⁶ <https://21cmfast.readthedocs.io/en/latest/>

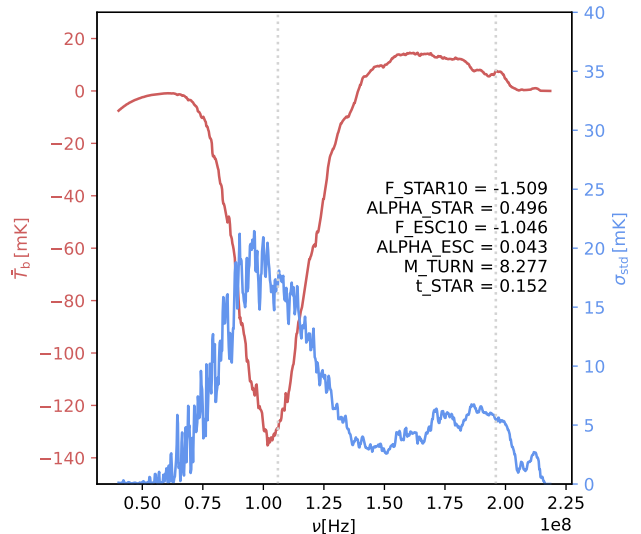


Figure 3. 21cmFAST parameters used for the generation of the EoR signal and corresponding mean (red) and standard deviation (blue) of the brightness temperature as a function of frequency. The vertical dotted lines represent the first and last frequency channel in the simulation.

scenario has been chosen since it is both physically plausible (given current observational constraints) and yields a strong CD/EoR signal over a wide frequency range, therefore providing good potential for detection and measurement. The resulting physical lightcone is in Figure 4. At the highest redshifts (lowest frequencies) there is CD signal, where x_{HI} traces the matter density. At the lowest redshift (highest frequency) the signal is dominated by reionisation. The neutral fraction is $\sim 90\%$, 50% , 10% at $z = 9.6$, 6.8 and 6.3 ($\nu \sim 134$, 181 , 196 MHz), respectively.

The simulated EoR signal, in units of cubic Mpc, has been converted into observational quantities (deg, deg, MHz) by means of the `tools21cm` library⁷ and added to the coarse grid.

4. ERROR MODEL

4.1. Partial de-mixing of out-of-field sources

The out-of-field sources introduced in Sec. 3.1.1 would normally be modelled and removed with a so-called “de-mixing” process within a calibration and imaging pipeline. Within our simulation these sources are attenuated by the OSKAR station beam as defined Sec. 2. However, as noted there, our use of identical rather than fully diverse station layouts yields significantly higher far-side-lobe levels, by about a factor of 10 on average, than would actually be the case. The visibility response to these sources will therefore be enhanced by this factor in the simulation. Our modelling of the de-mixing process (summarised in Table 3 of Braun 2019) suggests that only the brightest 10 - 20 discrete sources above the local horizon will need to be included in the de-mixing process and we might realistically anticipate achieving a net reduction of their effects by a factor of $\sim 10^{-2}$. Since inclu-

⁷ <https://tools21cm.readthedocs.io/>

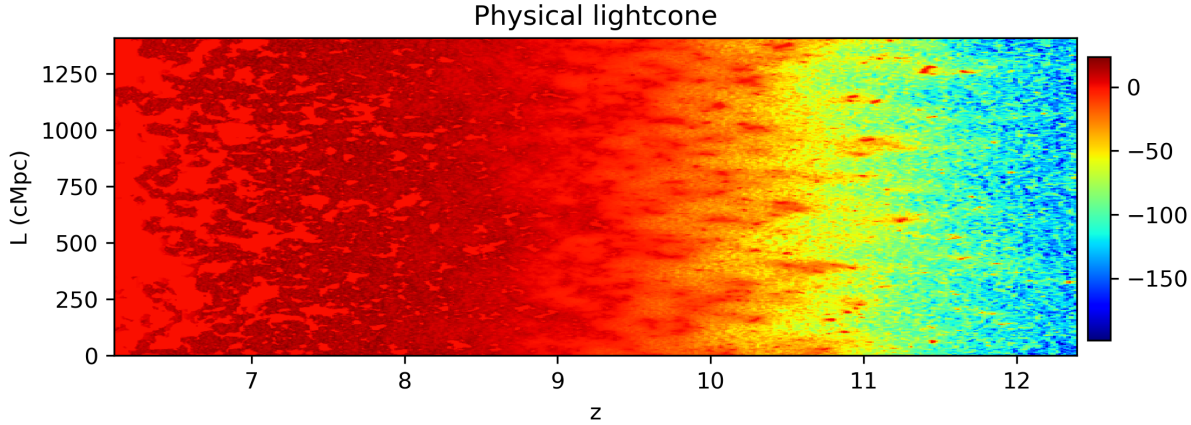


Figure 4. Lightcone in physical quantities corresponding to the chosen reionisation scenario over the redshift range of the simulation.

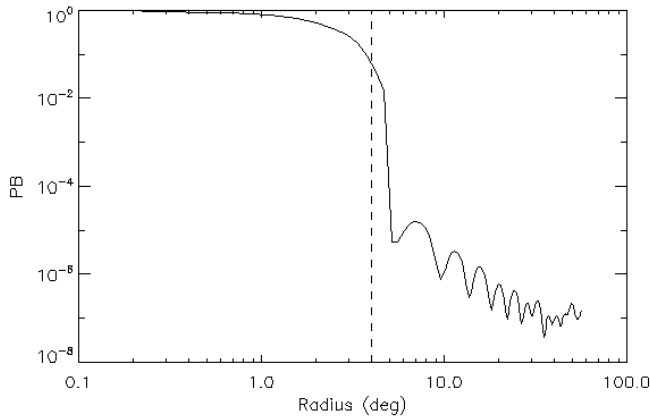


Figure 5. Primary beam response at 106 MHz, which shows the effective side-lobe level used to represent successful de-mixing. The vertical line shows the edge of the 8×8 deg field.

sion of an actual de-mixing pipeline was deemed beyond the scope of our current simulation efforts, we have instead attempted to approximate the net effect of both the presence of out-of-field sources as well as their partial de-mixing by defining an “effective” primary beam response, whereby the Sky Model is attenuated at large radii by a factor of 10^{-3} relative to the OSKAR station beam to take account of both of these effects. The effective primary beam response is shown in Fig. 5. Although this far-field attenuation factor is acknowledged to be quite arbitrary in magnitude, we have explored its plausibility by running subsets of the simulation with both larger and smaller factors. Higher levels of attenuation completely eliminate the “pitch-fork” effect (Thyagarajan et al. 2015) seen in delay spectra due to residual out-of-field contamination, while lower levels of attenuation lead to much stronger contamination.

4.2. Ionospheric effects and DD calibration errors

Another challenge that must be overcome in observations of this type is the successful modelling and elimination of propagation effects introduced into the visibility

data by the ionosphere. We have used the ARatmospy⁸ (Srinath et al. 2015) code to construct an ionospheric model that was intended to represent moderately good observing conditions, characterised by a correlation scale, $r_0 = 7$ km. The code is used to construct a time evolving phase screen above the telescope site that introduces Direction Dependent (DD) calibration errors into the visibilities via OSKAR. Several ionospheric layers were simulated at plausible elevations, propagation speeds and propagation directions with a deliberately slow time evolution. It has been shown in Table 3 of Braun (2019) that successful DD self-calibration should be possible between 100 and 200 MHz using the expected density of compact background sources (about 3×10^4 in number exceeding 1.5 mJy of apparent flux density) with sufficient signal-to-noise per visibility within each four hour tracking observation. We can conservatively expect an improvement of the DD gain solutions by at least a factor of 10 in each observation. Since the total observing campaign being simulated consists of 250 repetitions of this basic four hour track and each should have uncorrelated ionospheric distortions, we can expect a further $\sqrt{250}$ improvement in the final DD calibration precision, over that obtained per track. We have attenuated the total electron counts of the single track observation and the corresponding phase modulation by the factor 10^{-2} as an estimate of this final outcome.

4.3. DI calibration errors

Another component of calibration pertains to the so-called Direction Independent (DI) gain calibration of the telescope stations as a function of both time and frequency. We have constructed a gain model for the telescope array which represents the amplitude and phase response of each of the 512 stations for every time interval and every frequency channel of the observation. We have fixed the mean amplitude response at unity and the mean phase response at zero, so that there are no systematic calibration errors, however an error distribution applies. The time and frequency fluctuations are assumed to be independent of each other and the gain error at each specific (time, frequency) is given by the complex

⁸ <https://github.com/shrieeks/ARatmospy>

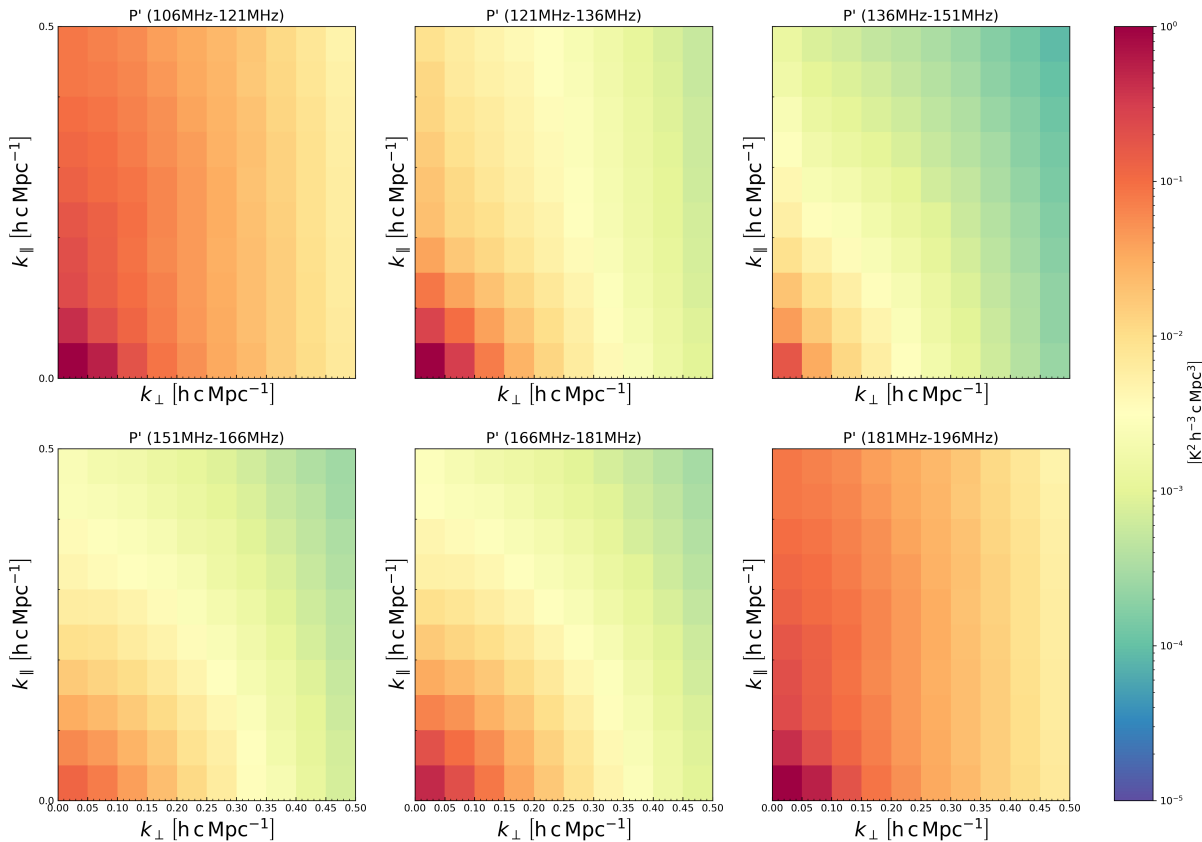


Figure 6. Cylindrical power spectrum of the true noiseless EoR, P' .

product of the two, one-dimensional distributions.

The one-dimensional gain distributions in each of time and frequency are first assigned random values from a Gaussian distribution with a specified standard deviation in each of amplitude and phase. We then make use of the `colorednoise` python code⁹ to take these “white-noise” distributions that have equal fluctuation power on all sampled scales and produce “red-noise” distributions with a -2 power-law index, whereby the greatest fluctuation power is present on the longest time intervals and over the largest frequency increments. Both the standard deviation and mean values are preserved in this process of colouring the noise. The resulting fluctuations are reminiscent of gain error patterns that are encountered in actual observations.

In assigning a numerical value to the standard deviation of the DI amplitude and phase errors we have considered both what might be realistically achieved for the calibration quality of a single observation as well as a plausible degree of improvement that might be achieved by averaging the outcomes of a large number of independent observations. Specifically, we have simulated a continuous four-hour duration tracking observation. However, we are using this to simulate the outcome of a 1000 hour deep integration, which would be achieved in practice by carrying out 250 repetitions of such a four-hour track. The relevant parameters for self-calibration of the DI gains are also shown in Table 3 of [Braun \(2019\)](#). We can expect to achieve an RMS calibration precision

of about ([Cornwell & Fomalont 1999](#)), $\phi = \sigma / (\sqrt{NS})$, where σ is the visibility noise per solution interval (about 1 Jy over 100 kHz and 60 sec ([Braun et al. 2019](#))), N is the number of stations (512) and S is the peak compact source brightness that occurs by chance within the field (about 20 Jy at 100 MHz). This yields an expected DI calibration precision of about 0.2 degrees of phase and 0.2% in amplitude for an individual track. After averaging over the 250 tracks we assume residual errors of 0.02 degrees in phase and 0.02% in amplitude for each of the time and the frequency domains. This is a reduction by a factor of 10 from the single track estimate, rather than the factor of 16 that would follow from $\sqrt{250}$, since we assume the solutions are not fully independent of one another, depending as they would on the same local sky model of the field. The time domain represents residual broadband gain calibration errors and the frequency domain represents residual bandpass calibration errors. While these estimates may prove to be optimistic, they at least provide a benchmark against which to assess the EoR signal recovery, and the simulation framework provides the means to test other circumstances.

4.4. Thermal noise

Finally we have added a level of thermal noise to the visibilities that is meant to represent the anticipated sensitivity of the system in conjunction with the total assumed integration time. What is provided to OSKAR is a file containing the SKA-Low station sensitivity expressed in units of Jy for a number of specific observing frequencies based on [Braun et al. \(2019\)](#). This nominal sensitiv-

⁹ <https://github.com/felixpatzelt/colorednoise>

ity per visibility, polarisation, unit bandwidth and unit time (about 1 Jy over 100 kHz and 60 sec) is then scaled for any possible differences between what is being simulated directly and what is being inferred. Specifically, only a single polarisation and four hour observation are being simulated directly, while the average of two polarisations and a total observing time of 1000 hours are being inferred. With this scaling in place, an appropriate thermal noise level is included in each visibility that is calculated.

4.5. Limitations

Although our EoR simulation provides an enhanced level of realism over previous work in this area, it is acknowledged to be far from complete. We have already drawn attention to several simplifications that were made to limit computational cost, including the use of only a single four-hour track to generate the visibility data, rather than the 250 repetitions of a track, each with distinct ionospheric conditions and its own DD and DI calibration challenges. Moreover, even this single track makes use of only a single station layout of antennas (rather than the 512 different variants that will be present) and only a single polarisation state of a highly idealised antenna element response. The deliberate diversity of both the station layouts and the nominal antenna polarisation states within the deployed SKA-Low is intended to regularise the instrumental response and reduce systematic errors. As noted in Sec. 2, OSKAR already provides support for the use of distinct station layouts and is anticipated to provide support for realistic embedded element patterns and non-cardinal alignment of the polarised response. It will be important to explore how these aspects of the deployed system flow through to the detectability of subtle astrophysical signals. Another aspect of our simulation that will be important to extend is our very approximate treatment of out-of-field sources. It's clear that out-of-field sources can dominate the visibility response at these low frequencies. As described in Sec. 4.1 we have modelled both the actual visibility response (from a distinct cross-correlation voltage beam for each visibility) as well as the process of successfully running a de-mixing pipeline by a simple attenuation of the auto-correlation station beam at large radii. This is acknowledged to be a very crude first step. The assumed far-field attenuation factor is at least available within the simulation code to allow further exploration of this phenomenon in the short term.

5. SIMULATED PRODUCTS

5.1. Simulated Visibilities

Visibilities are provided in the Measurement Set format, with every frequency channel being saved separately. The `casa` package¹⁰ (Team et al. 2022) was used to place the “SKA1-LOW” value into the “telescope” header with task `vishead`. The visibility data size amounts to 7.5 TB.

5.2. Simulated Images

The `wsclean` task¹¹ (Offringa et al. 2014) was used to produce images and the corresponding synthesised

beams (PSFs) from the visibilities, with natural weighting and no deconvolution. More specifically, the relevant `wsclean` parameters were: `-use-wgridder`, `-oversampling 4095`, `-kernel-size 15`, `-nwlayers 1000`, `-grid-mode kb`, `-taper-edge 100`, and `-padding 2`. These values were chosen to account for the intrinsically 3D data acquisition to yield an accurately position-invariant PSF. Once images and PSFs for all frequency channels were available, these were assembled into a cube. The `wsclean` specific fits header keywords are only preserved for the lowest frequency image that is assembled into each cube. The image cubes have a 2048×2048 pixels on a side which corresponds to a pixel size of 16×16 arcsec.

5.3. EoR products

Our list of products include the noiseless EoR signal, which can be used as a truth table to test foreground mitigation approaches. To this end we used the EoR cube in observational quantities derived at the end of Sec. 3. This has been smoothed to an effective resolution of 112×112 arcsec and sampled by 512×512 pixels, to reproduce the processing applied to all components in the coarse grid.

A set of 6 cylindrical (2D) and 6 spherical (1D) power spectra were computed with the `tools21cm` library on the noiseless EoR on 15 MHz frequency bins. The 2D EoR power spectra for all considered frequencies in shown in Fig. 6.

6. PRODUCT INSPECTION

Figure 7 shows the maps at 151 MHz (left panels) and the corresponding 2D power spectra between 151 and 166 MHz (right panels) for, from top to bottom, the clean EoR, the Galactic emission, and the total emission (EoR, Galactic and extragalactic emission, ionosphere). Instrumental effects (primary beam, PSF, calibration errors, etc.) are included in the total emission only. Colour scales for individual panels have been adjusted to allow inspecting each component, and are in general different. Note in particular that the clean EoR PS (top right) has a colour scale 6 orders of magnitude smaller than the Galactic and total PS components. To allow a comparison of the different amplitudes on the same scale, Fig. 8 shows the diagonal terms ($k_{\parallel} = k_{\perp}$ elements only) of the 2D power spectra of Figure 7.

Figures 7 and 8 illustrate and quantify the cumulative effect of multiple foreground components and instrumental effects on the EoR signal. The Galactic component alone (middle panels in Fig. 7 and dot-dashed line in Fig. 8) already dominates over the EoR signal at low ks , but leaves a relatively clean window for EoR detection over $k_{\parallel} \sim 0.1$ if instrumental effects are not considered. However, the addition of the extragalactic point sources introduces contamination at larger k_{\parallel} , and the ionosphere and instrumental effects cause contaminated modes to leak further into the cleaner part of the window (bottom panels of Fig. 7 and dashed line in Fig. 8).

While the current simulation does not fully capture the complexity of real data (see Sec. 4.5 for a list of the main simplifying assumptions), it constitutes a significant step forward with respect to most simulation work in the literature. It is therefore a useful benchmark against which to test foreground cleaning and avoidance methods that

¹⁰ <https://casa.nrao.edu/>

¹¹ <https://gitlab.com/aroffringa/wsclean>

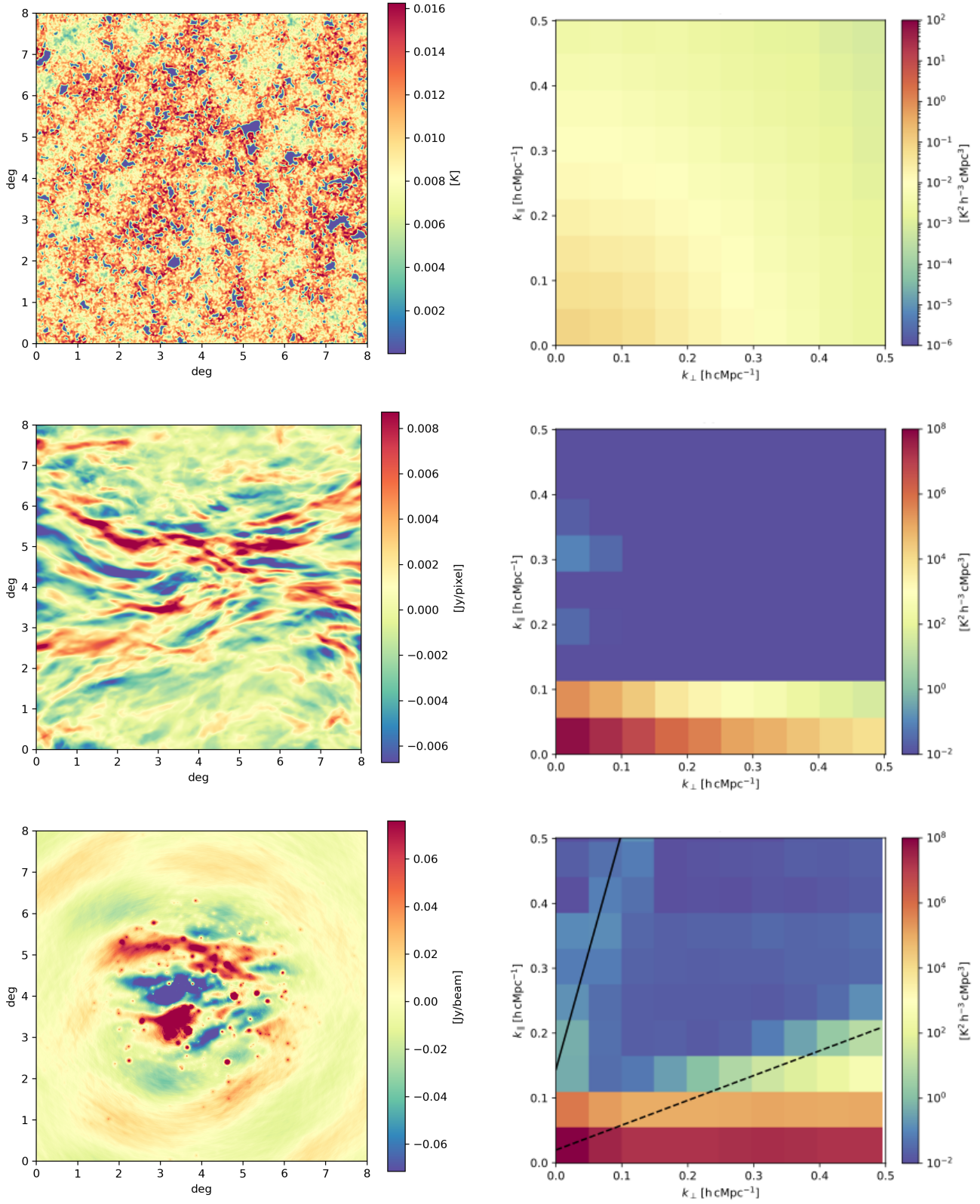


Figure 7. 151 MHz maps (left panels) and 2D power spectra at 151-166 MHz (right panels) of: EoR component (top), Galactic emission component (middle); total contribution of all emission components and instrumental response (bottom). Lines in the bottom-right panels represent the the horizon limit (solid black line) and the boundary corresponding to emission within the primary beam of the telescope (dashed black line).

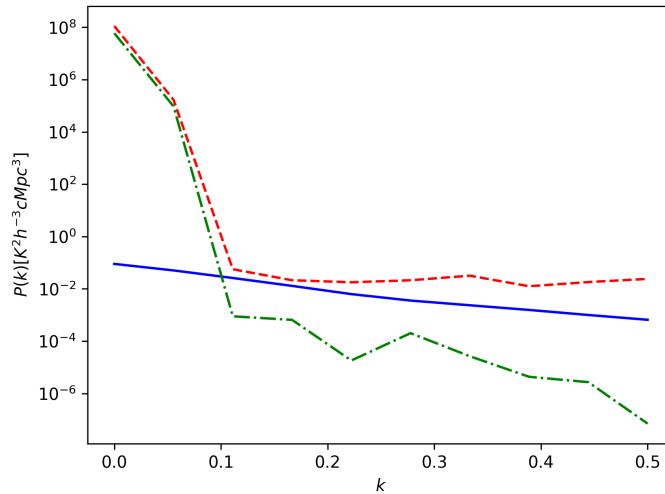


Figure 8. Diagonal terms ($k_{\parallel} = k_{\perp}$ elements only) of the 2D power spectra in the right panels of Figure 7: EoR component (solid line); Galactic emission component (dotted line); total contribution of all emission components and simulated instrumental response (dashed line). The EoR and the Galactic emission are presented as modelled and are free from simulated instrumental effects. The difference between the dotted line and the dashed line is therefore due to the combined effect of the EoR, the extragalactic sources, the ionosphere and the instrumental response.

are either being developed or applied to real data, as demonstrated by the SKA SDC3a data challenge (Bonaldi et al. 2025).

7. CONCLUSIONS

We have presented a comprehensive and realistic SKA-Low simulation designed to be used to assess the efficacy of EoR foreground-mitigation techniques. Our sky model includes the CD/EoR component generated with the `py21cmFAST` simulation package (Murray et al. 2020); Galactic foregrounds from the GSM2016 model (Zheng et al. 2017) and with small scales added above the native ~ 1 deg resolution with the MHD simulation presented in Bracco et al. (2022); strong out-of-field extragalactic sources and in-field sources from the Lynch et al. (2021) catalogue; faint extragalactic sources (down to $1 \mu\text{Jy}$ at 150 MHz) from the T-RECS (Bonaldi et al. 2019, 2023) simulation.

The telescope simulation was fully performed in the visibility domain with the `OSKAR` (Dulwich et al. 2009) code. The telescope configuration corresponds to the full SKA-Low array (512 stations, Dewdney & Braun 2016). A 4 h track was simulated, and the noise finally scaled to a 1000 h total integration.

Our simulation includes partial de-mixing of out-of-field strong sources; ionospheric effects generated with the `ARatmospy` (Srinath et al. 2015) software; DD and DI calibration errors. Imaging involved `wsclean` and further processing into power spectra used the `ps_eor` and `tools21cm` libraries.

The interaction between instrumental effects and the

sky signal is known to complicate the structure of the components both in the frequency and spatial domains, partially violating assumptions made by foreground-removal techniques. Those effects therefore need to be included to be able to test foreground mitigation in a realistic way. This simulation represents a step forward in this respect compared to previous work. As the basis of the SKA’s foreground mitigation data challenge, SDC3a (see Bonaldi et al. 2025, for a full description of the analysis and results) it has already yielded valuable lessons for the EoR data analysis community.

One of the outcomes of SDC3a is that multiple stages of analysis are needed to effectively decouple the different sources of complexity – point-source and diffuse foreground removal, and disentangling instrumental effects from sky signals. An iterative detection and subtraction of strong point sources before diffuse foreground removal, or an explicit deconvolution/convolution step to restore the smoothness of the components in the frequency dimension, achieved overall the best results in the challenge. Another outcome of the challenge is that error estimation is generally not robust enough at present against residual systematics after foreground mitigation.

The dataset released in this work, and the simulation framework published as a set of codes, can help further this research, as the community continues to pursue the detection of the EoR signal with currently operating and upcoming instrument, including the SKA.

8. DATA AVAILABILITY

The repositories used in this pipeline, including the scripts to reproduce this simulation, are listed in Table 1. Main dependencies include the `tools21cm`, `py21cmFAST`, `ps_eor` and `OSKAR` codes, as well as common astronomical packages.

The data cubes are available at <https://www.skao.int/en/science-users/170/simulated-data-products/ska-low-eor>.

9. ACKNOWLEDGEMENTS

AB and EL thank A. Mesinger, A. Nasirudin, S. Giri, B. Greig, G. Mellema, Y. Qin for useful advice and support in setting up the `21cmFAST` simulation. AB thanks M. Bianco and S. Giri for help and support with the `tools21cm` power spectrum estimation routines. FGM acknowledges support from the I-DAWN project, funded by the DIM-ORIGINS programme. ABracco acknowledges financial support from the INAF initiative “IAF Astronomy Fellowships in Italy” (grant name MEGASKAT). ABracco thanks V. Jelić, E. Ntormousi, and M. Padovani for their contribution to the diffuse Galactic foreground simulation.

REFERENCES

- Abdurashidova Z., et al., 2022, *ApJ*, **925**, 221
- Barry N., Hazelton B., Sullivan I., Morales M. F., Pober J. C., 2016, *MNRAS*, **461**, 3135
- Barry N., et al., 2019, *ApJ*, **884**, 1
- Bonaldi A., Bonato M., Galluzzi V., Harrison I., Massardi M., Kay S., De Zotti G., Brown M. L., 2019, *MNRAS*, **482**, 2
- Bonaldi A., Hartley P., Ronconi T., De Zotti G., Bonato M., 2023, *MNRAS*, **524**, 993
- Bonaldi A., et al., 2025, *arXiv e-prints*, p. [arXiv:2503.11740](https://arxiv.org/abs/2503.11740)
- Bowman J. D., Rogers A. E. E., Hewitt J. N., 2008, *ApJ*, **676**, 1

Table 1. Main repositories for our simulation pipeline.

| Code name | How is used in this pipeline | Repository Link |
|-------------------|--|---|
| SDC3a_repro | Main pipeline script and input files | https://github.com/abonaldi/SDC3a_repro |
| T-RECS | Generate catalogue of extragalactic sources | https://github.com/abonaldi/TRECS |
| SKAO-SDC | Create an image cube from the T-RECS catalogue | https://github.com/abonaldi/SKAO-SDC |
| SKA Low simulator | Consolidate all the sky components with OSKAR | https://github.com/omkarbait/ska-low-simulator |

- Bowman J. D., Rogers A. E. E., Monsalve R. A., Mozdzen T. J., Mahesh N., 2018, *Nature*, **555**, 67
- Bracco A., et al., 2022, *A&A*, **663**, A37
- Brackenhoff S. A., et al., 2024, *MNRAS*, **533**, 632
- Braun R., 2019, Technical report, SKA-TEL-SKO-0000941-02. SKA Organization
- Braun R., Bonaldi A., Bourke T., Keane E., Wagg J., 2019, *arXiv e-prints*, p. [arXiv:1912.12699](https://arxiv.org/abs/1912.12699)
- Chapman E., Jelić V., 2019, in 2514-3433, The Cosmic 21-cm Revolution. IOP Publishing, pp 6–1 to 6–29, [doi:10.1088/2514-3433/ab4a73ch6](https://doi.org/10.1088/2514-3433/ab4a73ch6), <https://dx.doi.org/10.1088/2514-3433/ab4a73ch6>
- Chapman E., et al., 2015, in Advancing Astrophysics with the Square Kilometre Array (AASKA14). p. 5 ([arXiv:1501.04429](https://arxiv.org/abs/1501.04429)), [doi:10.22323/1.215.0005](https://doi.org/10.22323/1.215.0005)
- Chokshi A., Barry N., Line J. L. B., Jordan C. H., Pindor B., Webster R. L., 2024, *MNRAS*, **534**, 2475
- Cornwell T., Fomalont E. B., 1999, in Taylor G. B., Carilli C. L., Perley R. A., eds, *Astronomical Society of the Pacific Conference Series Vol. 180, Synthesis Imaging in Radio Astronomy II*. p. 187
- Dewdney P. E., Braun R., 2016, Technical report, SKA-TEL-SKO-0000422. SKA Organization
- Dulwich F., Mort B. J., Salvini S., Zarb Adami K., Jones M. E., 2009, in *Wide Field Astronomy & Technology for the Square Kilometre Array*. p. 31, [doi:10.22323/1.132.0031](https://doi.org/10.22323/1.132.0031)
- Eastwood M. W., et al., 2019, *AJ*, **158**, 84
- Ewall-Wice A., et al., 2016, *MNRAS*, **460**, 4320
- Ewall-Wice A., Dillon J. S., Liu A., Hewitt J., 2017, *MNRAS*, **470**, 1849
- Garsden H., et al., 2021, *MNRAS*, **506**, 5802
- Hodgson T., Johnston-Hollitt M., 2026, *Astronomy and Computing*, **54**, 101012
- Jishnu Nambissan T., et al., 2021, *Experimental Astronomy*, **51**, 193
- Kolopanis M., et al., 2019, *ApJ*, **883**, 133
- Koopmans L., et al., 2015, in Advancing Astrophysics with the Square Kilometre Array (AASKA14). p. 1 ([arXiv:1505.07568](https://arxiv.org/abs/1505.07568)), [doi:10.22323/1.215.0001](https://doi.org/10.22323/1.215.0001)
- Li W., et al., 2019, *ApJ*, **887**, 141
- Lynch C. R., et al., 2021, *PASA*, **38**, e057
- Mertens F. G., et al., 2020, *Mon. Not. R. Astron. Soc.*, **493**, 1662
- Mertens F. G., Bobin J., Carucci I. P., 2024, *MNRAS*, **527**, 3517
- Mesinger A., Furlanetto S., Cen R., 2011, *MNRAS*, **411**, 955
- Munshi S., et al., 2024, *A&A*, **681**, A62
- Murray S., Greig B., Mesinger A., Muñoz J., Qin Y., Park J., Watkinson C., 2020, *J. Open Source Softw.*, **5**, 2582
- Ntormousi E., Dawson J. R., Hennebelle P., Fierlinger K., 2017, *A&A*, **599**, A94
- Offringa A. R., et al., 2014, *MNRAS*, **444**, 606
- Paciga G., et al., 2011, *MNRAS*, **413**, 1174
- Pal S. K., Datta A., Mazumder A., 2025, *J. Cosmology Astropart. Phys.*, **2025**, 058
- Patil A. H., et al., 2017, *ApJ*, **838**, 65
- Price D. C., 2016, PyGDSM: Python interface to Global Diffuse Sky Models, *Astrophysics Source Code Library*, record [ascl:1603.013](https://ascl.net/1603.013) ([ascl:1603.013](https://ascl.net/1603.013))
- Sault R. J., Teuben P. J., Wright M. C. H., 1995, in Shaw R. A., Payne H. E., Hayes J. J. E., eds, *Astronomical Society of the Pacific Conference Series Vol. 77, Astronomical Data Analysis Software and Systems IV*. p. 433 ([arXiv:astro-ph/0612759](https://arxiv.org/abs/astro-ph/0612759)), [doi:10.48550/arXiv.astro-ph/0612759](https://doi.org/10.48550/arXiv.astro-ph/0612759)
- Singh S., et al., 2017, *ApJL*, **845**, L12
- Srinath S., Poyneer L. A., Rudy A. R., Ammons S. M., 2015, *Optics Express*, **23**, 33335
- Team T. C., et al., 2022, *Publications of the Astronomical Society of the Pacific*, **134**, 114501
- Thyagarajan N., et al., 2015, *ApJL*, **807**, L28
- Trott C. M., Pober J. C., 2019, *arXiv e-prints*, p. [arXiv:1909.12491](https://arxiv.org/abs/1909.12491)
- Trott C. M., Wayth R. B., 2016, *PASA*, **33**, e019
- Trott C. M., et al., 2018, *ApJ*, **867**, 15
- Trott C. M., et al., 2020, *MNRAS*, **493**, 4711
- Vogel H., 1979, in *Math. Biosci.* p. 179, [doi:10.1016/0025-5564\(79\)90080-4](https://doi.org/10.1016/0025-5564(79)90080-4)
- Wilensky M. J., et al., 2023, *ApJ*, **957**, 78
- Wilensky M. J., et al., 2024, *RAS Techniques and Instruments*, **3**, 400
- Yoshiura S., et al., 2021, *MNRAS*, **505**, 4775
- Zheng H., et al., 2017, *MNRAS*, **464**, 3486

provides fast and easy peer review for new papers in the **astro-ph** section of the arXiv, making the reviewing process simpler for authors and referees alike. Learn more at <http://astro.theoj.org>.

This paper was built using the Open Journal of Astrophysics L^AT_EX template. The OJA is a journal which